A Quasi-2D Polypyrrole Film with Band-Like Transport Behavior and High Charge-Carrier Mobility

Kejun Liu, Julien Réhault, Baokun Liang, Mike Hambsch, Yingying Zhang, Sezer Seçkin, Yunxia Zhou, Rishi Shivhare, Peng Zhang, Miroslav Polozij, Tobias A. F. König, Haoyuan Qi, Shengqiang Zhou, Andreas Fery, Stefan C. B. Mannsfeld, Ute Kaiser, Thomas Heine, Natalie Banerji,* Renhao Dong,* and Xinliang Feng*

Quasi-2D (q2D) conjugated polymers (CPs) are polymers that consist of linear CP chains assembled through non-covalent interactions to form a layered structure. In this work, the synthesis of a novel crystalline q2D polypyrrole (q2DPPy) film at the air/H_2SO_4 (95%) interface is reported. The unique interfacial environment facilitates chain extension, prevents disorder, and results in a crystalline, layered assembly of protonated quinoidal chains with a fully extended conformation in its crystalline domains. This unique structure features highly delocalized π-electron systems within the extended chains, which is responsible for the low effective mass and narrow electronic bandgap. Thus, the temperature-dependent charge-transport properties of q2DPPy are investigated using the van der Pauw (vdP) method and terahertz time-domain spectroscopy (THz-TDS). The vdP method reveals that the q2DPPy film exhibits a semiconducting behavior with a thermally activated hopping mechanism in long-range transport between the electrodes. Conversely, THz-TDS reveals a band-like transport, indicating intrinsic charge transport up to a record short-range high THz mobility of ≈ 107.1 cm^2 V^{-1} s^{-1}.

1. Introduction

Linear conjugated polymers (CPs), such as polyacetylene, polypyrrole (PPy), and polythiophene, have played a crucial role in a range of electronic devices including organic light-emitting diodes,[1] transistors,[2] chemical (bio)sensors,[3] solar cells,[4] batteries,[5] and supercapacitors.[6] These applications require efficient charge transport but usually have to follow a thermally activated hopping transport mechanism due to potential barriers between local sites.[7] An alternative mechanism for charge transport in CPs is band-like transport, in which fully delocalized free carriers are subject to momentum scatterings (e.g., by phonons) to conduct along conjugated polymer chains. This transport mechanism is far more efficient

K. Liu, Y. Zhang, P. Zhang, M. Polozij, H. Qi, T. Heine, R. Dong, X. Feng
Faculty of Chemistry and Food Chemistry & Center for Advancing
Electronics Dresden
Technische Universität Dresden
01062 Dresden, Germany
E-mail: renhaodong@sdu.edu.cn; xinliang.feng@tu-dresden.de
K. Liu, J. Réhault, R. Shivhare, N. Banerji
Department of Chemistry and Biochemistry
University of Bern
Freiestrasse 3, Bern CH-3012, Switzerland
E-mail: natalie.banerji@unibe.ch
B. Liang, H. Qi, U. Kaiser
Central Facility of Materials Science Electron Microscopy
Universität Ulm
89081 Ulm, Germany

M. Hambsch, S. C. B. Mannsfeld
Center for Advancing Electronics Dresden and Faculty of Electrical and
Computer Engineering
Technische Universität Dresden
01062 Dresden, Germany
S. Seçkin, P. Zhang, T. A. F. König, A. Fery
Leibniz-Institut für Polymerforschung Dresden e.V. (IPF)
01069 Dresden, Germany
Y. Zhou, S. Zhou
Helmholtz-Zentrum Dresden-Rossendorf
Institute of Ion Beam Physics and Materials Research
Bautzner Landstraße 400, 01328 Dresden, Germany
T. Heine
Institute of Resource Ecology
Helmholtz-Zentrum Dresden-Rossendorf
Leipzig Research Branch, 04316 Leipzig, Germany
T. Heine
Department of Chemistry
Yonsei University
Seodaemun-gu, Seoul 120-749, South Korea

**ADVANCED
SCIENCE NEWS**

www.advancedsciencenews.com

**ADVANCED
MATERIALS**

www.advmat.de

than hopping transport, and researchers have made tremendous efforts to achieve band-like transport in CPs.[8] However, band-like transport in CPs is challenging due to the intrinsic disorder arising from chemical defects during polymerization and doping processes, which hinders the formation of long-range ordering and reduces carrier mobility, thereby limiting the performance of CP-based devices.[8g,9]

PPy is one of the most extensively studied CPs due to its remarkable stability, conductivity, and electroactivity. However, PPy is known to be always highly disordered due to the polymerization process, which can create defects in the polymer structure, leading to disorder in the conjugated backbone.[10] This disorder hinders the efficient movement of charge carriers through the polymer,[10a] making it difficult to achieve band-like transport. Additionally, the doping process used to tune the electronic properties of PPy can also introduce further disorder,[11] hindering the development of band-like transport in this material. Thus, even for some PPys with metal-like high conductivity, it is not necessarily an indication of band-like transport behavior[12] (see Figure S1, Supporting Information, for the example and discussion). Despite significant efforts to improve the charge-transport properties of PPy, band-like transport has not yet been reported for this material.[9c,d]

In this work, we report the synthesis of a novel quasi-2D polypyrrole (q2DPPy) film using an interface-assisted synthesis approach at an air/H_2SO_4 interface. The unique environment of this interface provided a confinement effect that facilitated chain extension and prevented disorder, resulting in a crystalline, layered assembly of protonated quinoidal chains with fully extended conformation. We then investigated the charge-transport properties of the q2DPPy film via van der Pauw (vdP) and terahertz time-domain spectroscopy (THz-TDS) measurements. We found that the long-range charge transport between electrodes was dominated by a hopping process and could be described by the Mott law variable-range hopping model. For the first time, our study reported distinctive band-like transport of PPy on the short range, as probed by the THz-TDS at low temperatures. This is related to more delocalized charge carriers that are more prone to take part in band-like transport at lower temperatures, as demonstrated by the evolution of the localization parameter (c_1) in the Drude–Smith model. The short-range, mainly intrachain charge transport in crystal domains or flakes, facilitated by the extended quinoidal chains within the layered q2DPPy film, contributed to this band-like transport behavior. Remarkably, a record-high short-range charge-carrier mobility of ≈ 107.1 cm^2 V^{-1} s^{-1} was achieved at 240 K.

R. Dong
Key Laboratory of Colloid and Interface Chemistry of the Ministry of Education
School of Chemistry and Chemical Engineering
Shandong University
Jinan 250100, China
X. Feng
Max Planck Institute of Microstructure Physics
Weinberg 2, D-06120 Halle, Sachsen-Anhalt, Germany

2. Results and Discussion

The oxidative polymerization of pyrrole was carried out as illustrated in **Figure 1**. Concentrated H_2SO_4 (95%) was injected into a glass petri dish with a diameter of 8 cm, followed by the dropwise addition of pyrrole (1 mL) onto the concentrated H_2SO_4 surface. After several drops, pyrrole polymerized and solidified at the interface of H_2SO_4 and air. The highly ordered 2D structure could be achieved via this interfacial synthesis, where pre-organization of monomer assemblies leads to long-range ordering in early reaction stages, serving as a precursor for subsequent crystalline polymer formation (Figures S2 and S3, Supporting Information). Excessive H_2SO_4 in the film was eliminated (as shown in Table S1, Supporting Information) by annealing the sample in iodine vapor at 80 °C overnight to form a dark film according to the literature method.[13] The resulting film was then heated in a vacuum at 80 °C to remove any remaining iodine residue, as characterized by X-ray photoelectron spectroscopy (XPS).

Figure 2a presents a large-area film (several cm^2) of q2DPPy with ≈ 2.2 μm thickness. The SEM images (Figure 2b and Figure S4, Supporting Information) and AFM image (Figure 2c) show a cross-section of a thick q2DPPy film with laminar morphology, which is similar to many inorganic 2D layered crystals (e.g., graphite[14] and MAX phase).[15] Notably, as shown in the inserted images in Figure 2b,c, the q2DPPy film could be exfoliated to produce nanosheets with an average lateral size of 28.3 ± 8.2 μm^2, and an average thickness of $\approx 4.5 \pm 0.3$ nm, corresponding to approximately four layers (Figures S5 and S6, Supporting Information, details of exfoliation process shown in the Supporting Information).

To clarify the crystal structure of q2DPPy, we performed grazing-incidence wide-angle X-ray scattering (GIWAXS) measurements on the q2DPPy film (Figure 2d and Figure S7 and Table S3, Supporting Information) and derived a unit cell with the following $a = 4.3$ Å, $b = 4.3$ Å, $c = 10.4$ Å, $\alpha = 94.7°$, $\beta = 86.4°$, and $\gamma = 115.2°$. The out-of-plane (001) peak indicates that there is an out-of-plane layer stacking with an average interlayer space of 10.3 Å. The complexity of the GIWAXS sample preparation process, which risks film delamination during rigorous washing steps, can lead to the potential entrapment of residual precursors within the film (detailed analysis can be found in the Supporting Information). These precursors were formed by self-assembly of protonated pyrrole or oligomers (Figures S2 and S3, Supporting Information). This indicates a pre-organization process playing a role in the formation of the crystalline q2DPPy, which will be elucidated in a further study. Aberration-corrected high-resolution transmission electron microscopy (AC-HRTEM) was employed to further investigate the structure of q2DPPy, as shown in Figure 2e. The AC-HRTEM image (Figure 2e and Figure S8, Supporting Information) and selected-area electron diffraction (SAED) patterns (top-left image inserted in Figure 2e) reveal a 2D lattice with an edge length of $a = b = 4.3$ Å and edge angle of $\gamma = 116°$, which agree well with the inserted chemical structure and its 3D models of fully extended quinoidal chains in Figure 2e.

In addition to experimental characterization, we also conducted HRTEM image simulations to gain a deeper understanding of the structure of q2DPPy, as shown in Figure S9, Supporting Information. The simulated HRTEM image provides

**ADVANCED
SCIENCE NEWS**

www.advancedsciencenews.com

**ADVANCED
MATERIALS**

www.advmat.de
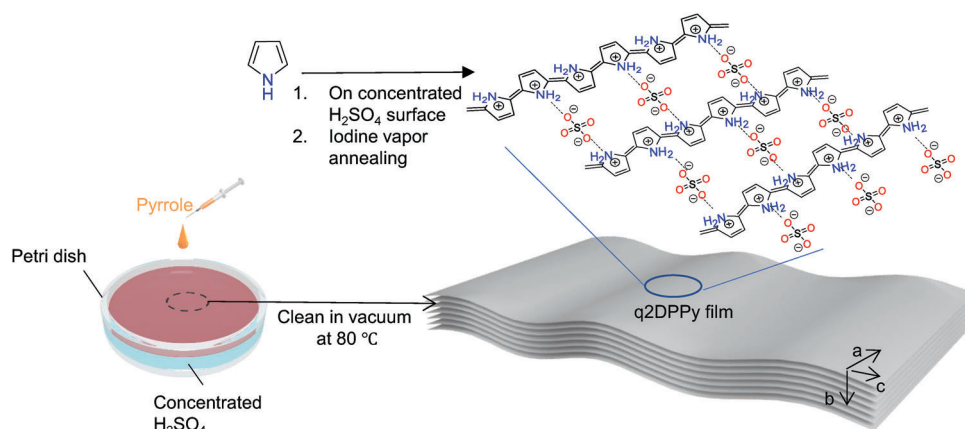
Figure 1. Schematic illustration and reaction scheme of the preparation of q2DPPy film on a concentrated H_2SO_4 surface.

an identical match to the experimental HRTEM image, revealing the diagonal direction of the lattice to be the direction of polymer chain extension, as labeled in Figure 2e. The lattice diagonal length of ≈7.4 Å matched the repeat unit length of the fully extended quinoidal chain structure in the crystalline regions, as shown in Figure S10 and Table S4, Supporting Information. The cross-section of the q2DPPy film was characterized by SAED, which showed an interlayer spacing of ≈10 Å (illustrated in Figure 2g), as indicated by the (001), (002), and (003) crystal planes in Figure 2f and Figure S11 and Table S6, Supporting Information. This interlayer distance is larger than the π-stacking distance due to the presence of sulfuric acid groups spacing or bridging between the two polymer chains.

To determine the chemical composition of q2DPPy, Fourier-transform infrared (FTIR) spectroscopy (**Figure 3**a) was performed. A major peak at 1650 cm^{-1} indicates the NH_2^+ deformation band in q2DPPy.[12b] Several other peaks at 1525 and 1440 cm^{-1} represent stretching vibrations of the pyrrole ring.[16] The S=O stretching mode of the interchain linkers (SO_4^{2-}) is seen as a broad and strong band centered at 1037 cm^{-1}.[17] Raman spectroscopy complements FTIR as it detects different molecular vibrations, offering a broader view of the chemical structure. Figure 3b shows two strong Raman peaks at 1584 and 1428 cm^{-1}. The 1584 cm^{-1} peak corresponds to the C=C ring stretching, similar to the G peak of graphene at ≈1580 cm^{-1}.[18] Another intense peak at 1428 cm^{-1} is attributed to the antisymmetric C—N stretching and C—H bending.[19] Overall, the FTIR and Raman spectroscopy results match the proposed structure of q2DPPy.

As shown in Figure 3c, the UV–vis–near-infrared (NIR) absorption spectrum of q2DPPy film shows a broad band in the VIS region (<750 nm), attributed to π → π* transition and mid-gap transition of polypyrrole,[20a,b] and further bands in the NIR range (800 to 2500 nm). The NIR range can be divided into several sub-ranges, such as NIR-I (650–950 nm), NIR-II (1100–1350 nm), NIR-III (1600–1870 nm), and NIR-IV (centered at 2200 nm).[20c,d] Reported PPy spectra generally display broad absorbance in the NIR-I and NIR-II regions, which is attributed to the bipolarons in PPy.[12b,20d] Compared to those reports,[12b,20d] Figure 2c shows that the absorption of q2DPPy film is redshifted to the NIR-III and NIR-IV regions with peaks at 1936, 2140, and 2262 nm,

attributed to delocalized polaron band, as calculated by Ullah and et al.[20b] This absorption disappears when the films are partially de-doped in acetone (Figure S12, Supporting Information). The low-bandgap absorption is comparable to some prominent inorganic NIR absorber materials such as antimony tin oxides[21] and indium tin oxides.[22] It reflects a narrow optical bandgap of oxidized q2DPPy film, which is attributed to excitation from its valance band to the delocalized polaron band.[20b]

The XPS spectra (Table S5, Supporting Information) of q2DPPy reveal the presence of N, S, and O elements in the film, with a ratio of N/S/O = 2.1/1/4.3, which closely matches the theoretical ratio of 2/1/4. The iodine content in the film is negligible (<1%). The C1s main peak in Figure 2d exhibits three singlets at 284.5, 285, and 286.6 eV. The peaks at 284.5 and 285 eV are attributed to the β- and α-carbons of the pyrrole rings,[18c] respectively, while the peak at 286.6 eV arises from the protonated structure of PPy.[23] The N1s spectrum (Figure 3e) exhibits a bimodal feature that can be deconvoluted into two singlets at 400.5 and 402 eV, corresponding to the —NH_2^+— and C—N$^+$ species, respectively (Figure 2e).[18b,c] These XPS results confirm the presence of the expected elements and chemical bonding in the q2DPPy film.

To investigate the transport mechanism of q2DPPy, we employed both the vdP and THz-TDS methods at variable temperatures. The vdP method provides the long-range charge-carrier conductivity at a macroscopic scale between electrodes spaced 1 cm apart, under a constant current of 100 nA. According to the vdP results depicted in **Figure 4**a,b (blue circles), the charge transport follows a semiconducting feature and is dominated by thermally activated hopping in the temperature range from 300 K (with $\sigma_{vdP, 300 K} = 0.54$ S cm^{-1}) to around 250 K. This data could be fit linearly with the Mott law variable-range hopping model, which takes the form $\sigma_{hopping} = \sigma_0 e^{-(T_0/T)^{1/4}}$. However, the conductivity values at $T < 250$ K were near the detection limit of the vdP experiment, which resulted in scattering data points and deviation from the linear fitting.

For a further understanding, the electronic structure of the fully extended quinoidal polypyrrole chains was investigated using theoretical calculations with the PBE+D3(BJ) method,[24] revealing a bandgap of 0.42 eV (Figure 4c), in agreement with the red-shifted absorbance bands. This is smaller than that of the
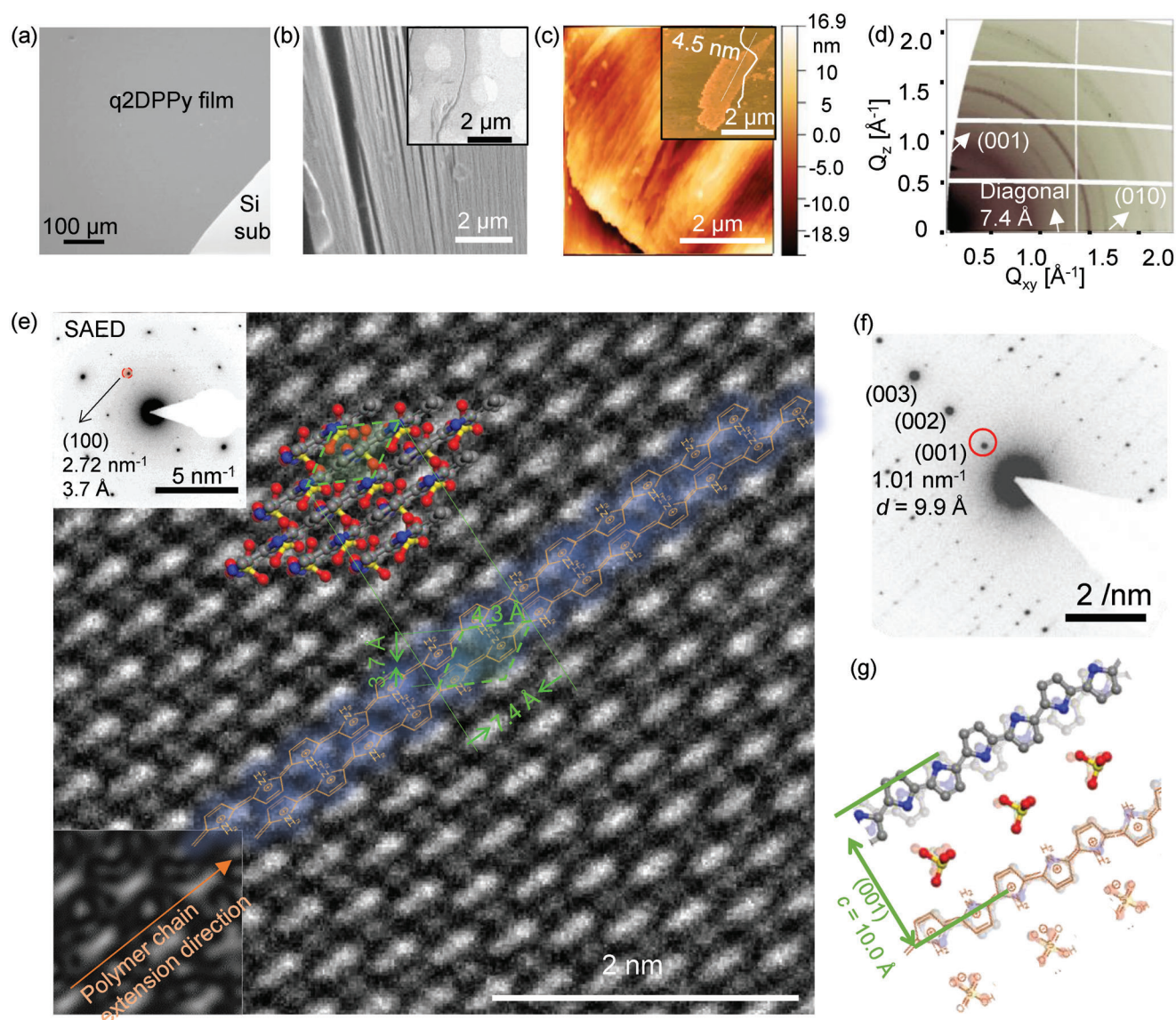
ADVANCED
SCIENCE NEWS

www.advancedsciencenews.com

ADVANCED
MATERIALS

www.advmat.de

Figure 2. Morphological and structural analysis of the q2DPPy film. a) SEM image from a top-view direction. b) SEM image and c) AFM image from a cross-section direction with inserted images of exfoliated flake in the top-right corner of the images. d) 2D GIWAXS pattern of q2DPPy. e) AC-HRTEM image of q2DPPy with inserted SAED pattern (upper-left); and a simulated (bottom-left) HRTEM image matching the experimental image; the proposed chemical quinoidal PPy chain structure is overlapped in the image with lattice parameters. f) SAED pattern and g) PPy chain stacking schematic from the cross-section direction of the film.

pristine unprotonated PPy (3.2 ± 0.1 eV).[9c] The bandgap narrowing is attributed to the formation of new energy bands in the protonated, fully extended quinoidal polypyrrole chains.[9c] The effective mass along the extended chains in q2DPPy is calculated based on the band structure (Figure 4c), yielding $m^* = 0.44\ m^0$, much lower than previous reports of PPy ($m^* = 1.8\ m^0$).[25] In q2DPPy films, the increased planarity arising from the fully extended quinoidal chains within the layers enhances charge delocalization, leading to a lower effective mass and enhanced charge-transport properties.

Then, we employed temperature-dependent THz-TDS to characterize the local charge transport within the picosecond terahertz field.[8c,26] Figure 4d shows the raw data of the detected electric field intensity through q2DPPy films, which shows an intensity drop from 300 to 200 K. It reveals that the absorption of THz radiation by q2DPPy film is enhanced at lower temperatures, indicating an increase in conductivity.[27] To quantify the conductivity σ_{THz}, we further converted the plots of Figure 4d to the frequency-dependent refractive index ($n(\omega)$) and absorption coefficient ($\alpha(\omega)$), which in turn could be represented as the complex conductivity function with real and imaginary parts as shown in Figure 4e.

We found that both the real and imaginary parts of the complex conductivity function increased with decreasing temperature in Figure 4e and Figure S13, Supporting Information, which confirm an increase in σ_{THz}. To analyze how σ_{THz} changes with tem-
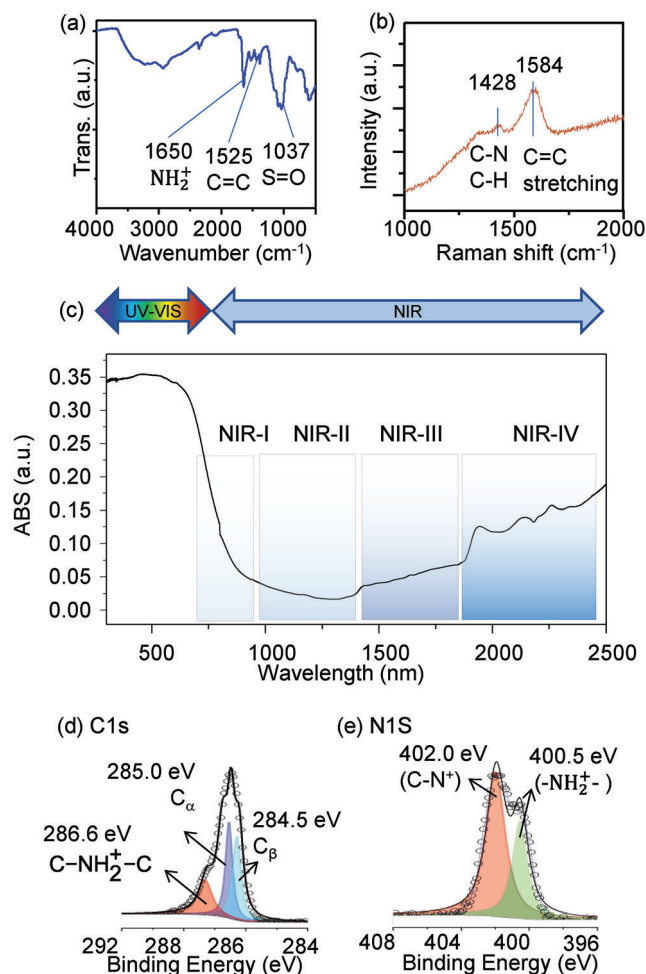
Figure 3. Characterization of the chemical composition of q2DPPy. a) FTIR spectrum showing characteristic peaks of functional groups of q2DPPy. b) Raman spectrum of q2DPPy. c) UV–vis–near-infrared (NIR) absorbance spectrum obtained with an integrating sphere to minimize scattering effects during our measurements. d,e) High-resolution XPS spectra of C1s (d) and N1s (e).

resents the in-chain direction and has the lowest effective mass ($m^* = 0.44\ m^0$), showing that this direction represents the main transport direction in the THz measurements (Table S9, Supporting Information). The effective mass in the in-plane direction of π-stacked polymer chains ($\Gamma\rightarrow N$) is an order of magnitude higher and therefore has a weak (but non-negligible) contribution to transport. Finally, $\Gamma\rightarrow B$ characterizes the out-of-plane direction, highlighting the path of charge hopping from one PPy chain through the sulfate ions to another PPy chain, and this shows very ineffective charge transport. Thus, at the molecular level, THz-TDS captures the local transport that occurs predominantly along the chains within short timeframes (<10 ps), while the macroscopic conductivity is characterized by the vdP method, which reveals a thermally activated hopping mechanism for long-range transport between electrodes. The observed difference between short-range THz and long-range vdP conductivity reflects differing underlying phenomena at various length scales of the material structure, a behavior that has been noted in stacked 2D materials due to inherently less efficient charge transport across multiple layers compared to a single isolated flake.[26]

For a better understanding of the complex conductivity of q2DPPy, we fit the complex conductivity spectra using the Drude–Smith model for both real and imaginary parts at various temperatures as shown in Figure S13, Supporting Information (including all temperatures), and Figure 4e (seven temperatures are selected for clarity). In the Drude–Smith model, the complex conductivity is described by

$$\tilde{\sigma}(\omega) = \frac{\varepsilon_0\omega_{\mathrm{p}}^2\tau}{1-i\omega\tau}\left[1+\frac{c_1}{1-i\omega\tau}\right] \tag{1}$$

where ω_{p} is the plasma frequency, ε_0 is the free space permittivity, τ is the scattering time, and c_1 is the persistence of velocity or localization parameter. The c_1 parameter pertains to the likelihood of charge carriers to be scattered after a collision at boundaries. Its value ranges between 0 and -1, with 0 indicating the restoration of the Drude model and the presence of free charges, while the lower limit -1 indicates strongly localized charges. We found that c_1 of the q2DPPy film is negative and decreases further with the increase of temperature (becomes more negative), as shown in the inset of Figure 4f and Table S6, Supporting Information. It exhibits a gradual change from -0.89 at 299 K to -0.86 at 290 K and then rises faster from -0.86 to -0.70 in the range of 290 to 260 K. Below 260 K, the increase in the c_1 parameter is more significant, reaching a value of -0.57 at 240 K. Overall, the data suggest that the localization of charge carriers becomes weaker with decreasing temperature, which leads to a lower probability of backscattering after a collision at boundaries. The scattering time τ is associated with local band-like transport within polymer chain segments or aggregates.[8a,26,28] The scattering time exhibits fluctuations around an average value of ≈104 fs across various temperatures, yet it displays an overall increasing trend from 94.8 ± 7 fs (300 K) to 116.1 ± 7.1 fs (240 K), as shown in Table S7, Supporting Information. This trend implies that the charge carriers have an extended distance of motion before experiencing collisions with any boundaries or obstacles at low temperatures.

Furthermore, we calculated the effective short-range mobility according to $\mu_{\mathrm{eff}} = e\tau/(m_0(1+c_1))$, using the calculated effective

perature, we computed the average and standard deviation of the real part of complex conductivity data points ranging from 0.8 to 1.2 THz. These values were then plotted in Figure 4b to compare them with the long-range conductivity obtained by the vdP method. As shown in Figure 4b (square symbols), the THz conductivity remains constant (with weak fluctuations around 7.75–7.87 S cm^{-1}) in the range from 300 to 260 K. It then shows a steady increase from 260 to 240 K (9.09 ± 0.23 S cm^{-1}), indicating band-like conductivity in this temperature range. However, an opposite trend, $d\sigma_{\mathrm{vdP}}/dT > 0$, is detected by the vdP method, as shown in Figure 4b. The discrepancy can be explained by the difference between the vdP method, which measures long-range charge-carrier conductivity across different flakes or crystalline domains, and the THz-TDS technique, which characterizes local charge transport in individual crystallites. To further understand the local transport mechanism, we theoretically elucidated the effective mass along different directions in the first Brillouin zone of q2DPPy (Figure S15, Supporting Information). $\Gamma\rightarrow Q$ rep-
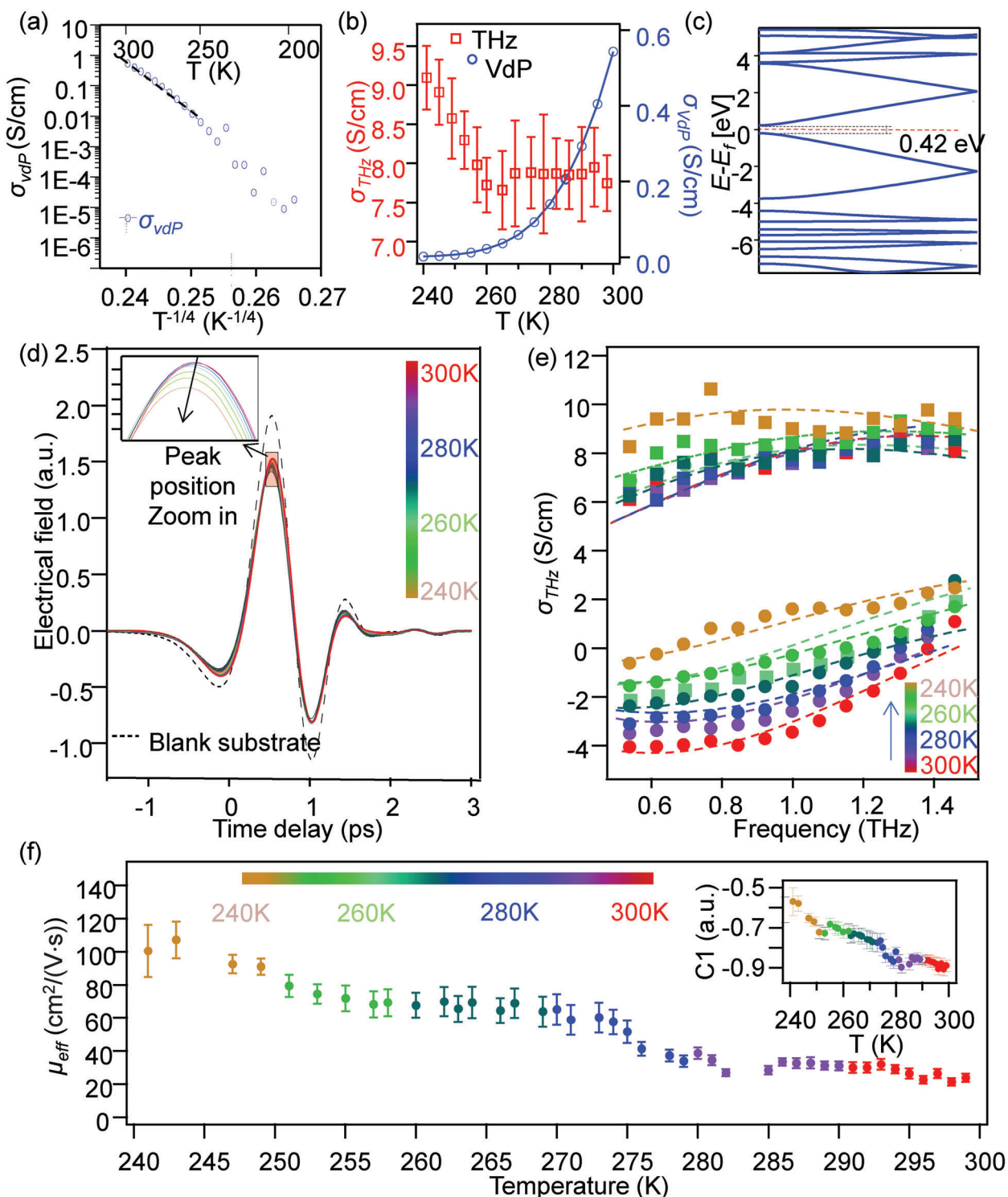
Figure 4. Charge-transport study of the q2DPPy film. a) Semilogarithmic plot of electrical conductivity measured by the vdP method versus $T^{-1/4}$ over the measured temperature range, with a linear fit using the Mott law variable-range hopping model between 300 and 250 K. b) Temperature-dependent conductivity from the THz and vdP methods. For clarity, one data point was selected for every 2 K interval by extracting the real part of THz-TDS conductivity between 0.8 and 1 THz. c) Electronic band structure along the Γ–X path line in the first Brillouin zone for a single protonated fully extended quinoidal chain. d) THz-TDS traces of the time-resolved electrical field intensity (solid lines) and reference THz pulse (blank, dashed line) at temperatures ranging from 240 to 298 K under inert gas (N_2) conditions. e) Complex THz conductivity spectra at 299, 290, 280, 269, 250, and 241 K are shown in different colors. The Drude–Smith model fits their real (square symbol ■) and imaginary (circle symbol ●) parts are represented as dashed lines. f) Effective THz mobility at various temperatures according to $\mu_{eff} = q\tau/(m_o(1 + c_1))$, with the inserted figure showing the c_1 value at different temperatures.

2303288 (6 of 8)

**ADVANCED
SCIENCE NEWS**

www.advancedsciencenews.com

**ADVANCED
MATERIALS**

www.advmat.de

mass for intrachain transport. Figure 4f shows that the effective mobility of q2DPPy exhibits a negative correlation with temperature, which is indicative of band-like transport behavior. At a temperature of 300 K, the short-range mobility is $\mu_{299K} = 23.9 \pm 2.5$ cm^2 V^{-1} s^{-1} and gradually increases to a remarkable value of $\mu_{243K} = 107.1 \pm 11$ cm^2 V^{-1} s^{-1} at a temperature of 243 K. This trend of increasing short-range mobility is mainly attributed to the increase of the c_1 parameter with the decrease of temperature (inset of Figure 4f). It should be emphasized that the measured highest short-range mobility of 107.1 cm^2 V^{-1} s^{-1} represents a new record value among reported polypyrrole-based materials (the literature reported mobility of PPys is typically below 15 cm^2 V^{-1} s^{-1}) as shown in Table S8, Supporting Information. Finally, we also identify significant Coulomb trapping effects induced by the sulfate anions in q2DPPy. This reflects in the low density of mobile charge carriers contributing to the THz conductivity ($1.22 \pm 0.12 \times 10^{18}$ cm^{-3} at 299K according to Drude–Smith analysis), despite the important doping level revealed by UV–vis-NIR spectroscopy. The low mobile carrier density explains the relatively low σ_{THz} (<10 S cm^{-1}) in spite of the high local mobility. Moreover, the mobile charge-carrier density demonstrates a decline with decreasing temperature, indicating the thermal activation of charge carriers in q2DPPy (Figure S14, Supporting Information), as evidenced by the carrier densities at 299 ($1.2 \pm 0.04 \times 10^{18}$ cm^{-3}) and 236 K ($0.92 \pm 0.04 \times 10^{18}$ cm^{-3}). This trapping effect can also impede macroscopic charge transport. It can be mitigated by substituting the sulfate ions with other larger aromatic linkers (Figure S1, Supporting Information), where we observed an over tenfold increase in the local conductivity.

3. Conclusion

We have reported the synthesis of a novel q2DPPy film via oxidation-induced polymerization at the air/H_2SO_4 interface, resulting in a unique layer-stacked 2D morphology. The structure of each layer consists of protonated, fully extended, and quinoidal PPy chains with a very low bandgap (<0.5 eV). Due to high order within crystalline domains, we identified band-like intra-chain transport of q2DPPy, with increasing carrier mobility and delocalization at low temperatures. Remarkably, a record high short-range mobility of 107.1 cm^2 V^{-1} s^{-1} for PPy materials at 240 K was achieved. Further research is needed to extend the excellent intrinsic transport properties to the long-range (between individual flakes) and to overcome Coulomb trapping by the sulfonate ions. For the latter, we show important improvement when using large aromatic ions instead. In a future study, we will further explore the band-like transport behavior in such q2DPPy materials, with a focus on temperatures closer to room temperature and long-range transport.

Supporting Information

Supporting Information is available from the Wiley Online Library or from the author.

Conflict of Interest

The authors declare no conflict of interest.

Data Availability Statement

The data that support the findings of this study are available from the corresponding author upon reasonable request.

[1] M. S. White, M. Kaltenbrunner, E. D. Głowacki, K. Gutnichenko, G. Kettlgruber, I. Graz, S. Aazou, C. Ulbricht, D. A. M. Egbe, M. C. Miron, Z. Major, M. C. Scharber, T. Sekitani, T. Someya, S. Bauer, N. S. Sariciftci, *Nat. Photonics* **2013**, *7*, 811.

[2] S. Wang, J. Xu, W. Wang, G.-J. N. Wang, R. Rastak, F. Molina-Lopez, J. W. Chung, S. Niu, V. R. Feig, J. Lopez, T. Lei, S.-K. Kwon, Y. Kim, A. M. Foudeh, A. Ehrlich, A. Gasperini, Y. Yun, B. Murmann, J. B. H. Tok, Z. Bao, *Nature* **2018**, *555*, 83.

[3] a) J. Janata, M. Josowicz, *Nat. Mater.* **2003**, *2*, 19; b) F. Wei, Y. Zhong, H. Luo, Y. Wu, J. Fu, Q. He, J. Cheng, J. Na, Y. Yamauchi, S. Liu, *J. Mater. Chem. A* **2021**, *9*, 8308.

[4] B. H. Lee, S. H. Park, H. Back, K. Lee, *Adv. Funct. Mater.* **2011**, *21*, 487.

[5] C. Wang, W. Zheng, Z. Yue, C. O. Too, G. G. Wallace, *Adv. Mater.* **2011**, *23*, 3580.

[6] L. Pan, G. Yu, D. Zhai, H. R. Lee, W. Zhao, N. Liu, H. Wang, B. C.-K. Tee, Y. Shi, Y. Cui, Z. Bao, *Proc. Natl. Acad. Sci. USA* **2012**, *109*, 9287.

[7] a) S. T. Keene, W. Michaels, A. Melianas, T. J. Quill, E. J. Fuller, A. Giovannitti, I. McCulloch, A. A. Talin, C. J. Tassone, J. Qin, A. Troisi, A. Salleo, *J. Am. Chem. Soc.* **2022**, *144*, 10368; b) E. Hendry, M. Koeberg, J. M. Schins, H. K. Nienhuys, V. Sundström, L. D. A. Siebbeles, M. Bonn, *Phys. Rev. B* **2005**, *71*, 125201.

[8] a) M. Ballabio, T. Zhang, C. Chen, P. Zhang, Z. Liao, M. Hambsch, S. C. B. Mannsfeld, E. Zschech, H. Sirringhaus, X. Feng, M. Bonn, R. Dong, E. Cánovas, *Adv. Funct. Mater.* **2021**, *31*, 2105184; b) J. Lee, J. W. Chung, D. H. Kim, B.-L. Lee, J.-I. Park, S. Lee, R. Häusermann, B. Batlogg, S.-S. Lee, I. Choi, I. W. Kim, M. S. Kang, *J. Am. Chem. Soc.* **2015**, *137*, 7990; c) Y. Mei, P. J. Diemer, M. R. Niazi, R. K. Hallani, K. Jarolimek, C. S. Day, C. Risko, J. E. Anthony, A. Amassian, O. D. Jurchescu, *Proc. Natl. Acad. Sci. USA* **2017**, *114*, E6739; d) T. Sakanoue, H. Sirringhaus, *Nat. Mater.* **2010**, *9*, 736; e) U. Salzner, *Wiley Interdiscip. Rev. Comput. Mol. Sci.* **2014**, *4*, 601; f) P. Venezuela, M. Lazzeri, F. Mauri, *Phys. Rev. B* **2011**, *84*, 035433; g) Y. Yamashita, J. Tsurumi, F. Hinkel, Y. Okada, J. Soeda, W. Zajączkowski, M. Baumgarten, W. Pisula, H. Matsui, K. Müllen, J. Takeya, *Adv. Mater.* **2014**, *26*, 8169.

[9] a) D. Farka, H. Coskun, J. Gasiorowski, C. Cobet, K. Hingerl, L. M. Uiberlacker, S. Hild, T. Greunz, D. Stifter, N. S. Sariciftci, R. Menon, W. Schoefberger, C. C. Mardare, A. W. Hassel, C. Schwarzinger, M. C. Scharber, P. Stadler, *Adv. Electron. Mater.* **2017**, *3*, 1700050; b) R. Noriega, A. Salleo, A. J. Spakowitz, *Proc. Natl. Acad. Sci. USA* **2013**, *110*, 16315; c) K. Lee, E. K. Miller, A. N. Aleshin, R. Menon, A. J. Heeger, J. H. Kim, C. O. Yoon, H. Lee, *Adv. Mater.* **1998**, *10*, 456; d) R. S. Kohlman, J. Joo, Y. Z. Wang, J. P. Pouget, H. Kaneko, T. Ishiguro, A. J. Epstein, *Phys. Rev. Lett.* **1995**, *74*, 773; e) O. Bubnova, Z. U. Khan, H. Wang, S. Braun, D. R. Evans, M. Fabretto, P. Hojati-Talemi, D. Dagnelund, J.-B. Arlin, Y. H. Geerts, S. Desbief, D. W. Breiby, J. W. Andreasen, R. Lazzaroni, W. M. Chen, I. Zozoulenko, M. Fahlman, P. J. Murphy, M. Berggren, X. Crispin, *Nat. Mater.* **2014**, *13*, 190.

[10] a) M. Xue, F. Li, D. Chen, Z. Yang, X. Wang, J. Ji, *Adv. Mater.* **2016**, *28*, 8265; b) M. Pandey, K. Deshmukh, *J. Appl. Polym. Sci.* **2022**, *139*, e52450; c) R. Yang, W. H. Smyrl, D. F. Evans, W. A. Hendrickson, *J. Phys. Chem.* **1992**, *96*, 1428.

[11] A. B. Kaiser, *Adv. Mater.* **2001**, *13*, 927.

[12] a) W. Kim, H.-J. Lee, Z. Ahmad, S. J. Yoo, Y.-J. Kim, S. Kumar, M. Changez, J.-S. Lee, J.-S. Lee, *Nanoscale* **2019**, *11*, 15641; b) H.-J. Lee, Y.-R. Jo, S. Kumar, S. J. Yoo, J.-G. Kim, Y.-J. Kim, B.-J. Kim, J.-S. Lee, *Nat. Commun.* **2016**, *7*, 12803; c) J. Park, Y. Lee, M. Kim, Y. Kim, A. Tripathi, Y.-W. Kwon, J. Kwak, H. Y. Woo, *ACS Appl. Mater. Interfaces* **2020**, *12*, 1110.

[13] J. Arotsky, H. C. Mishra, M. C. R. Symons, *J. Chem. Soc.* **1962**, 2582.

[14] a) K. Parvez, Z.-S. Wu, R. Li, X. Liu, R. Graf, X. Feng, K. Müllen, *J. Am. Chem. Soc.* **2014**, *136*, 6083; b) S. Yang, M. R. Lohe, K. Müllen, X. Feng, *Adv. Mater.* **2016**, *28*, 6213.

[15] M. R. Lukatskaya, O. Mashtalir, C. E. Ren, Y. Dall'Agnese, P. Rozier, P. L. Taberna, M. Naguib, P. Simon, M. W. Barsoum, Y. Gogotsi, *Science* **2013**, *341*, 1502.

[16] G. G. Mastantuoni, V. C. Tran, I. Engquist, L. A. Berglund, Q. Zhou, *Adv. Mater. Interfaces* **2023**, *10*, 2201597.

[17] T. I. Yacovitch, T. Wende, L. Jiang, N. Heine, G. Meijer, D. M. Neumark, K. R. Asmis, *J. Phys. Chem. Lett* **2011**, *2*, 2135.

[18] a) A. C. Ferrari, J. C. Meyer, V. Scardaci, C. Casiraghi, M. Lazzeri, F. Mauri, S. Piscanec, D. Jiang, K. S. Novoselov, S. Roth, A. K. Geim, *Phys. Rev. Lett.* **2006**, *97*, 187401; b) C. Malitesta, I. Losito, L. Sabbatini, P. G. Zambonin, *J. Electron. Spectrosc. Relat. Phenom.* **1995**, *76*, 629; c) L. M. Santino, Y. Diao, H. Yang, Y. Lu, H. Wang, E. Hwang, J. M. D'Arcy, *Nanoscale* **2019**, *11*, 12358.

[19] S. Demoustier-Champagne, P.-Y. Stavaux, *Chem. Mater.* **1999**, *11*, 829.

[20] a) P. Rapta, A. Neudeck, A. Petr, L. Dunsch, *J. Chem. Soc., Faraday Trans.* **1998**, *94*, 3625. b) H. Ullah, A.-u.-H. A. Shah, S. Bilal, K. Ayub, *J. Phys. Chem. C* **2014**, *118*, 17819. c) M. Vasilopoulou, A. Fakharuddin, F. P. García de Arquer, D. G. Georgiadou, H. Kim, A. R. b. Mohd Yusoff, F. Gao, M. K. Nazeeruddin, H. J. Bolink, E. H. Sargent, *Nat. Photonics* **2021**, *15*, 656; d) M. Šišáková, Y. Asaumi, M. Uda, M. Seike, K. Oyama, S. Higashimoto, T. Hirai, Y. Nakamura, S. Fujii, *Polym. J.* **2020**, *52*, 589.

[21] J. M. Xu, L. Li, S. Wang, H. L. Ding, Y. X. Zhang, G. H. Li, *CrystEngComm* **2013**, *15*, 3296.

[22] J. Wu, C. Mu, J. Yang, *Sci. Rep.* **2020**, *10*, 12808.

[23] T. M. Townsend, A. Allanic, C. Noonan, J. R. Sodeau, *J. Mater. Chem. A* **2012**, *116*, 4035.

[24] S. Grimme, S. Ehrlich, L. Goerigk, *J. Comput. Chem.* **2011**, *32*, 1456.

[25] K. Lee, R. Menon, C. O. Yoon, A. J. Heeger, *Phys. Rev. B* **1995**, *52*, 4779.

[26] a) W. Zheng, B. Sun, D. Li, S. M. Gali, H. Zhang, S. Fu, L. Di Virgilio, S. Li, S. Yang, S. Zhou, D. Beljonne, M. Yu, X. Feng, H. I. Wang, M. Bonn, *Nat. Phys.* **2022**, *18*, 544; b) R. Dong, P. Han, H. Arora, M. Ballabio, M. Karakus, Z. Zhang, C. Shekhar, P. Adler, P. S. Petkov, A. Erbe, S. C. B. Mannsfeld, C. Felser, T. Heine, M. Bonn, X. Feng, E. Cánovas, *Nat. Mater.* **2018**, *17*, 1027.

[27] a) K. J. Tielrooij, J. C. W. Song, S. A. Jensen, A. Centeno, A. Pesquera, A. Zurutuza Elorza, M. Bonn, L. S. Levitov, F. H. L. Koppens, *Nat. Phys.* **2013**, *9*, 248; b) R. Ulbricht, E. Hendry, J. Shan, T. F. Heinz, M. Bonn, *Rev. Mod. Phys.* **2011**, *83*, 543.

[28] P. Krauspe, D. Tsokkou, M. Causa, E. Buchaca-Domingo, Z. Fei, M. Heeney, N. Stingelin, N. Banerji, *J. Mater. Chem. A* **2018**, *6*, 22301.